Artificial coloration of ancient agate beads: a mineralogical study

Xiaoguang Li[1], Haozhong Xue[1,2], Xinhua Wu[3], Dahai Qin[4], Daiming Chen[4], Jiangyan Yuan[1] and Zihua Tang[5*]

Abstract

The process of staining was frequently employed to enhance or alter the color of agate beads in ancient times. One of the key challenges in studying ancient beads is comprehending the intricate techniques employed to color agate stones. An understanding of the staining mechanism from a mineralogical standpoint offers insights into the level of technological advancement in different civilizations. In this study, the mineral structure of eight ancient agate beads from Xinjiang Uygur Autonomous Region, NW China, was analyzed using Micro X-ray fluorescence (μXRF), Raman spectroscopy, Scanning Electron Microscope (SEM), and Fourier Transform Infrared (FTIR) techniques. The color, transparency, mineral phase, and surface roughness of the beads were examined, revealing variations ranging from colorless to light violet to dark violet. Raman and FTIR spectroscopy were employed to determine the SiO_2 phase and the changes in optical characteristics of agate beads after artificial staining. The black color of the beads was formed by carbon penetration, while the red color was produced by heating. The coexistence of α-quartz and moganite phases in the red, the dark red, the black, the idiochromatic white and the part translucent zones of the ancient beads was confirmed by the 464 cm^{-1} peak of α-quartz and the 502 cm^{-1} peak of moganite phase. The analyzed red, the dark red, the black, the idiochromatic white and the part translucent zones exhibited remarkably similar FTIR spectral features, with two prominent bands at ~1097 and ~1187 cm^{-1}, as well as two weak bands at 798 and 778 cm^{-1}, indicating the presence of moganite and α-quartz in the unetched ancient beads. In contrast to the idiochromatic white appearance of natural agate, the scattered white coloration in etched beads was generated by an etching reaction. Both Raman and FTIR spectroscopy indicated the absence of moganite in etched beads, indicating that the scattered white color was produced by the loss of moganite and a portion of α-quartz, resulting in a rough surface.

Keywords Ancient beads, Carnelian, Agate, α-quartz, Moganite

*Correspondence:
Zihua Tang
tangzihua@mail.iggcas.ac.cn
[1] State Key Laboratory of Lithospheric Evolution, Institute of Geology and Geophysics, Chinese Academy of Sciences, Beijing 100029, China
[2] University of Chinese Academy of Sciences, Beijing 100049, China
[3] Institute of Archaeology, Chinese Academy of Social Sciences, Beijing 100101, China
[4] Xinjiang Archeological Team, Institute of Archaeology, Chinese Academy of Social Sciences, Korla 841001, China
[5] Key Laboratory of Cenozoic Geology and Environment, Institute of Geology and Geophysics, Chinese Academy of Sciences, Beijing 100029, China

Introduction

The etched and colored agate beads, as a daily decoration, religious decoration, or indicators of power and status for ancient people, were excavated in many ancient cultural locations such as Arabia, Persian Gulf, and Asia [1–15]. Etched or stained beads were defined as a type of carnelian or chalcedony with a manufactured coloration pattern [1, 2, 4, 16]. In China, most etched or stained beads were unearthed from Xinjiang Uygur Autonomous Region, Tibet Autonomous Region, Yunnan Province, Guangdong Province, Henan Province, and Qinghai Province [17–20].

Li *et al. Heritage Science*   (2023) 11:195

Page 2 of 12

Previous studies decades ago [2, 3, 8, 21–26] have illustrated the shape, design, drilling technique, and color of the ancient beads. The beads chosen as ancient ornaments obviously underwent a series of different handicraft staining, which may indicate a symbolic and economic value. Previous studies have also found that the designed pattern changes over time and excavated regions, although there may be commercial activity conducted among the ancient civilizations at different locations [5, 10, 27–30]. Hence, excavated beads from different historical periods reflect craftsmanship advances and indicate craft skills development.

To a certain extent, the color styles of the ancient beads affect the appreciation of the people of the spreading destination through cultural infiltration. With the development of the urban society and technical expertise, natural pattern with simple surface polishing cannot express the motif of the elite communities [29]. The beads have changed dramatically during their spreading period, which covers the Neolithic Period around 7000 B.C. to the Early Historic Period [16, 29, 31]. One of the essential characteristics is the color, which can be correlated to the diverse line patterns of the beads. With the development of manufacturing, advances in agate beads-making technology resulted in new colors and various color patterns, such as white, red, and black [1, 4, 32, 33]. Pioneering works have divided colors of ancient beads into three color types: type I white-on-red, type II black-on-white, and type III black-on-red. Type I is the most common type, while black-on-white was less discovered. Type III was extremely rare. Artificial color patterns of the ancient beads can reflect the source area, production age, and handicraft development level. Differentiating the artificial origin color from natural color is the priority in the coloration research of the ancient beads. Therefore, interpreting the mineral character and the methods of manufacturing color is crucial for further research.

Agate mainly consists of microcrystalline quartz with a chemical composition of SiO_2 and Mohs hardness of 6.5–7. Naturally produced agate can show various colors with waxy lustre, generally colorless or translucent due to the difference of various trace elements [34–36]. It is usually a difficult task to differentiate the manufactured color and idiochromatic color by optical observation. For the black-on-white type, it was considered that the beads were whitened entirely at the first step and then drawn with a metallic solution [4, 16, 37]. Human-controlled heat treatment plays a significant role in the red coloration manufacturing process [22]. Experimental research showed that the white line of type I comes from alkali solution etching [4, 16, 31, 37]. However, SiO_2 was believed to have low reactivity. The terms etching, bleaching, and painting were used when describing the

manufacturing mechanism of the white color [2, 4, 16, 38]. How do different mineral phases and colors respond differently to artificial staining? Illustrating the staining mechanism allows us to analyze humans' manufacture and intellectual level at that time [22, 24, 30, 33].

Raman and FTIR spectroscopy are non-destructive and have been employed to identify mineral polymorphs and analyze mineral structure [17, 39–44]. The µXRF allowed us to in-situ identify the element composition of the mineral. SEM helps to investigate the coarseness of the beads' surface. Here, we studied eight ancient beads with different color types by µXRF, FTIR, Raman, and SEM techniques at a micrometer scale. The staining mechanism was revealed from a mineralogical perspective.

Experimental

Samples

The Jirzankal Cemetery, which is approximately 2500 years old, takes its name from the tableland on the eastern Pamir Plateau where it is located. Situated in SW Xinjiang, China, the cemetery shares borders with Tajikistan, Afghanistan, Pakistan, and India to the west, providing significant potential for western connections. During the extensive excavations carried out between 2013 and 2015, a range of exotic objects were discovered in the cemetery. For example, musical instruments such as harps found in burials M14 and M16 likely originated from the Near East, while silk fabrics discovered in burials M1 and M2 may have been transported from the eastern part of China [45]. Additionally, a variety of bone, glass, and agate beads discovered in the cemetery suggest broader connections with various cultures. Of these, 81 agate beads marked the cemetery as the largest bead-buried cemetery of its time in China. These beads exhibit various colors, both natural and artificial, and display intricate designs, providing valuable insights into the coloration of ancient agate beads.

This study focuses on eight agate beads excavated from burials BM11, BM14, BM23, and BM32, see Fig. 1. Among them, one bead is a plain red carnelian bead (H: BM23:12-7), four are etched carnelian beads with various white designs (A: BM32:7-6, E: BM14:9-1-8, F: BM23:12-1, G: BM11:22-2), and three are striped beads with pale and dark parallel layers (B: BM32:7-3, C: BM32:7-4, and D: BM11:22-1). These beads represent the major designs of agate beads found in China.

Instrumentation and operating conditions

Raman spectroscopy was performed at room temperature using a Witec alpha300R confocal Raman microscope at the Institute of Geology and Geophysics, Chinese Academy of Sciences (IGGCAS). The laser beam was focused
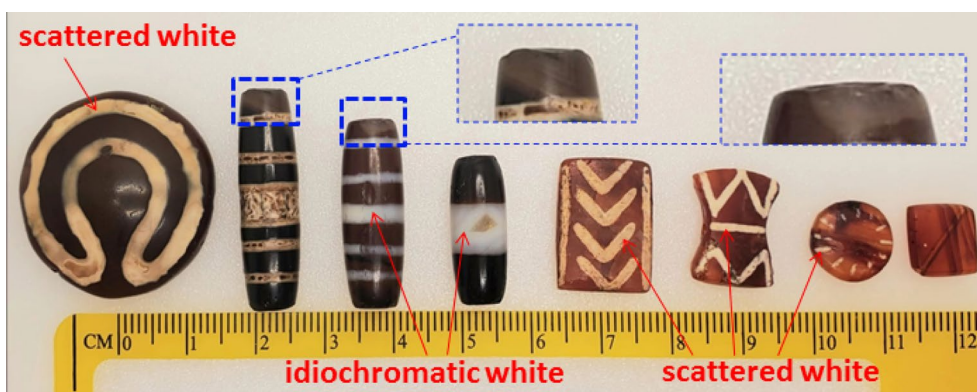
Li *et al. Heritage Science*   (2023) 11:195

Page 3 of 12

Fig. 1 The eight ancient beads from Jirzankal cemetery, Xinjiang, NW China. (From left to right, BM32:7-6, BM32:7-3, BM32:7-4, BM11:22-1, BM14:9-1-8, BM23:12-1, BM11:22-2, and BM23:12-7 were labeled as A–H)

on the sample surface using a 50×Zeiss microscope (NA=0.75). The Raman data has been calibrated with a silicon peak of 520.7 cm^{-1}. The spectra were collected with a 488 nm laser with a spectral acquisition time of 1 s and 60 accumulations for each measurement. The investigated spectra range from 100 to 4500 cm^{-1} using 300 grooves/mm optical grating. At least ten measurements were operated for one sample.

FTIR spectra were collected using a Bruker Vertex 70 V spectrometer at IGGCAS. A Hyperion 2000 IR microscope with an MCT detector cooled with liquid nitrogen connected to the Bruker Vertex 70 V spectrometer was used to obtain the microscopy IR spectra. Spectra were acquired from a single 100×100 μm spot on each analysed point. Background spectra were collected from a gold mirror. The FTIR spectra were recorded using reflectance mode with the co-addition of 64 scans between 650 and 4000 cm^{-1} at a resolution of 1 cm^{-1}.

A Zeiss Gemini 450 electron microscope instrument at IGGCAS was used to study the morphology of the surface of the beads. The SE images were collected from the original surface. Samples for SEM measurement were not coated with carbon or any metal. The SE images were acquired at 2 kV accelerating voltage and beam current of 200 pA and working distance of 8.5 mm. The SEM was carried out under 3.01×10^{-6} mbar vacuum conditions.

MicroXRF experiments were performed on the Bruker M4 TORNADO plus μXRF spectrometer at IGGCAS, which enables the detection and analysis of the entire element range from carbon to americium. A dual silicon drift detector (30 mm^2) measures X-rays with a resolution < 145 eV measured on Mn-Kα at a spatial resolution of ~20 μm [46]. In this study, all the scanning μXRF element mapping experiments were performed with an X-ray tube energy of 50 kV and a current of 600 μA, with 8 ms per pixel spectrum acquisition time and a pixel step-size of 18 μm. Data analyses, including obtaining elemental maps on all objects and quantitative XRF analysis from zone of interest, were undertaken with the characterization software provided by Bruker Micro Analytics.

Results and discussion

Optical appearance

Table. 1 shows the optical characteristics of the beads. Our visual observations of all the studied beads showed roughly faceted oval shapes with rounded edges. The most noticeable characteristic of the beads is the color and pattern. The dark red and black beads were transparent and showed a dull lustre, while the dark red and black beads were part translucent and showed a greasy lustre. The B and C beads feature a translucent zone located at the head of the beads(yellow rectangle schematic in Figs. 1, 2). Of all the color types, the white-on-red variety was the most common. According to Beck's division of the prevailing era of the beads type, their pattern characteristics show the producing age of

Table 1 Optical characteristics of the eight studied beads

Sample number	Configuration	Color	Transparency
A	Plain	Scattered white, Dark red	Translucent
B	Banded beads	Scattered white, Black	Mainly opaque, Part translucent
C	Banded beads	idiochromatic white, Dark red	Translucent
D	Banded beads	idiochromatic white, Black	Part translucent
E	Plain	Scattered white, Red	Translucent
F	Plain	Scattered white, Red	Translucent
G	Plain	Scattered white, Red	Translucent
H	Plain	Red	Transparent

Li *et al. Heritage Science*   (2023) 11:195
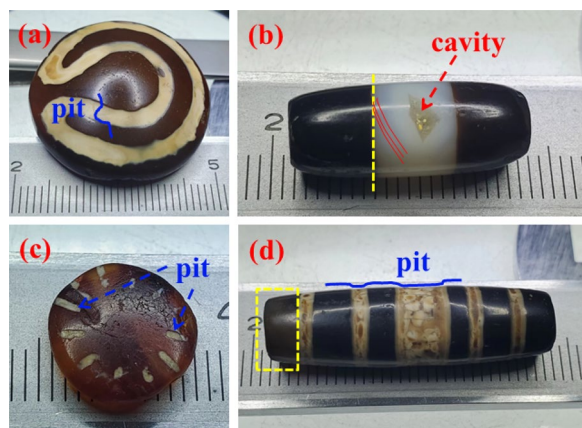
Page 4 of 12

Fig. 2 **a**, **c**, **d**: Optical graph shows the pit of the scattered white zone, **b** Optical graph shows the cavity and the white layers were cut by the edge of the black zone

approximately 2300 years, which is consistent with the dating results of the cemetery [2, 12, 14, 47, 48]. The carnelian beads E, F, G, and H were translucent and showed a vitreous lustre. They varied from white ('scattered white' or 'idiochromatic white', see Fig. 1 and Section "Idiochromatic white and scattered white") to light red to dark red to black (Table 1).

Figure 2 shows that the scattered white zones of samples A, B, and G are pits. The light red, the dark red, the black, and the idiochromatic white zones are flat and smooth compared with the scattered white zone. The scattered white line covers the flat surface with a distance range from approximately 0.5 mm (Sample G) to 6.0 mm (Sample B). The idiochromatic white gel layers and the cavity of the sample D are seen without artificial alteration [49, 50]. The extension trend of the white layers with different degrees of whiteness was cut by the edge of the black zone (Fig. 2-b).

µXRF

All samples contained Si, O, Na, K, Ca, and Fe. Si and O account for 98wt.% of the elements in weight percent (Table 2), indicative of the chemical composition of the α-quartz mineral [51]. The scattered white zone contains significantly more Na and Ca than other color zones. This artificial staining process must have used some Na-containing and Ca-containing liquid—for example, plants and calcium carbonate minerals. K is evenly distributed across samples at a lower content. Based on the µXRF data (Table. 2) and optical microscope observation (Figs. 1,2), Fe is uniformly distributed in samples A and B, while the Fe measured by the other four carnelians (E, F, G, and H) show irregular distribution on its surface. Therefore, higher Fe content (0.04%) was observed (Table. 2).

Raman spectra

All beads exhibited the characteristic Raman peaks of α-quartz at 464 cm^{-1} and weak peaks at 128 and 207 cm^{-1}. The 464 cm^{-1} is the strongest Raman peak assigned to the vibration of the SiO_4 six-membered ring, and the 128 and 207 cm^{-1} peaks were assigned to Si-O-Si bending vibrations of α-quartz microcrystalline [52]. The shoulder at 502 cm^{-1} corresponds to symmetric stretching vibrations of the four-membered Si-O-Si ring, which was proved to be moganite by previous Raman studies [52–55]. All the Raman spectra in Fig. 3 and the spectra of the idiochromatic white zone of B-b, C, and D (Fig. 4) confirmed the presence of moganite. This indicates that the moganite and microcrystalline quartz coexists in the original agate stone materials of beads. According to the integral ratio of the 502 cm^{-1} and 465 cm^{-1} bands [56], the moganite content of all the studied samples is in the range 0 to 50wt%.

The distinct Raman peaks demonstrate that the black zone of samples A and D is formed due to artificial alteration without breaking the main chemical bond (Figs. 2,

Table 2 Chemical compositions of the different color zones

[norm. at.%] Sample zone	Si	O	Na	K	Ca	Fe
A Dark red zone	35.9	63.5	0.36	0.05	0.08	0.03
A Scattered white zone	35.8	63.3	0.68	0.05	0.22	0.03
B Black zone	35.9	63.6	0.38	0.07	0.06	0.03
B Scattered white zone	35.7	63.2	0.75	0.08	0.19	0.03
F Red zone	35.9	63.4	0.39	0.08	0.11	0.04
F Scattered white zone	35.9	63.4	0.35	0.09	0.16	0.04
E Red zone	35.98	63.54	0.32	0.05	0.06	0.04
E Scattered white zone	35.85	63.28	0.59	0.07	0.17	0.04
H Red zone	35.88	63.68	0.28	0.05	0.07	0.04

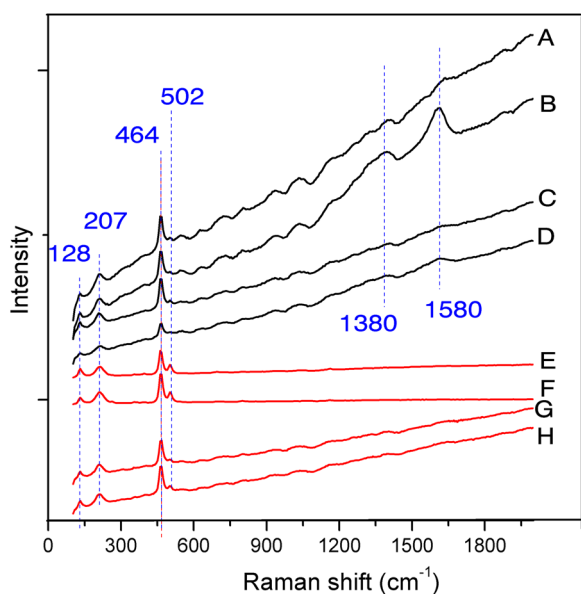Li *et al. Heritage Science*   (2023) 11:195

Page 5 of 12

Fig. 3 Raman spectra of A dark red zone, B black zone, C dark red zone, D black zone, E red zone, F red zone, G red zone, and H red zone
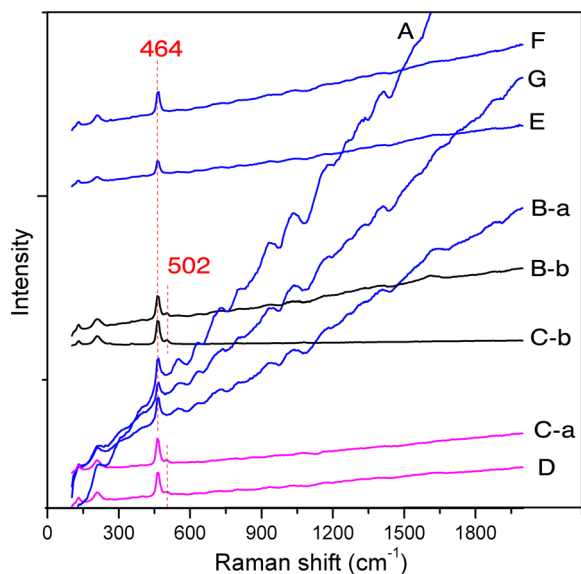

Fig. 4 Raman spectra of A scattered white zone, B-a scattered white zone, B-b part translucent zone, C-a idiochromatic white zone, C-b part translucent zone, D idiochromatic white zone, E scattered white zone, F scattered white zone, and G scattered white zone

3, 4). Also, two relatively strong bands were distinctly observed at 1380 and 1580 cm^{-1}, which are absent in the spectra of most of the red and white zones. These features can be interpreted as the D and the G peaks of disordered carbon [57, 58]. The minor carbon content could account for the dark red and black color of A and D

samples, respectively. For the spectra of the white zone, no carbon was detected except sample B.

In the part translucent zones of B and C (Dashed rectangle symbol shown in Figs. 1, 2), the intensity of the Raman peaks is much stronger than any other zone (Fig. 4), indicating a low-defect quartz structure with less intercrystalline porosity [56]. As a result, a zone with a higher crystallinity degree could accommodate less exotic elements. This indicates that the crystallinity degree of the translucent zones is much greater, which in turn prevents the staining process.

Selected Raman spectra collected from the scattered white zone of the beads are shown in Fig. 4. It can be seen that the moganite peak is absent. However, the moganite peak was still observed from spectra collected from the idiochromatic white zone of samples C and D.

Raman spectra of the irregularly distributed red dots at the surface of the sample E (Fig. 5) confirmed the presence of hematite, with peaks centered at 229, 299, and 409 cm^{-1} [59, 60].

FTIR spectra
The red, the dark red, the black, the idiochromatic white and the part translucent zones of all of the samples show similar FTIR patterns with two prominent absorption
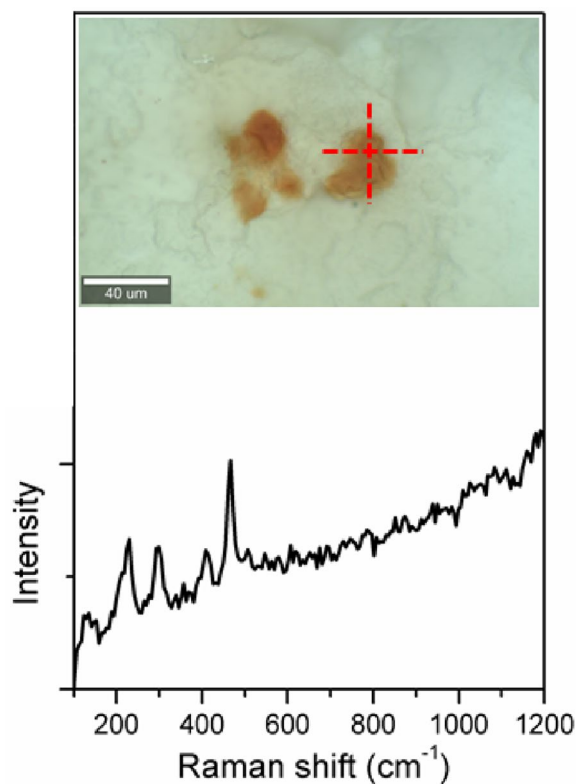

Fig. 5 Raman spectra of the red dot of sample E

bands at ~ 1097 and ~ 1187 cm^{-1} and two weak absorption bands at 798 and 778 cm^{-1} (Figs. 6, 7), which can be assigned to the asymmetric stretching vibration of Si-O and symmetric stretching vibration of Si-O-Si, respectively [44, 60–62]. FTIR bands indicate that the mineral composition of the red and black zones are characteristic of agate and contain a low amount of moganite (Fig. 6) [63]. The band ratio of 1097 cm^{-1} peak and the trough at 1158 cm^{-1} is sensitive to the abundance of moganite [56]. However, this parameter only works well for high moganite content samples (more than 50%) [56].

For the scattered white zone, the two prominent peaks show a redshift to the low wavenumber region. A sharp absorption band is observed at ~ 1084 cm^{-1}, and a subtle band at 1180 cm^{-1}. These bands are expected to be mainly associated with Si-O stretching vibrations of α-quartz [64]. Moganite was considered to be an unstable precursor mineral of α-quartz in previous studies [44, 65–67], and there may be a tendency for a slow transition to quartz in natural environments. This is why moganite is easier to be etched at high temperatures. Unlike
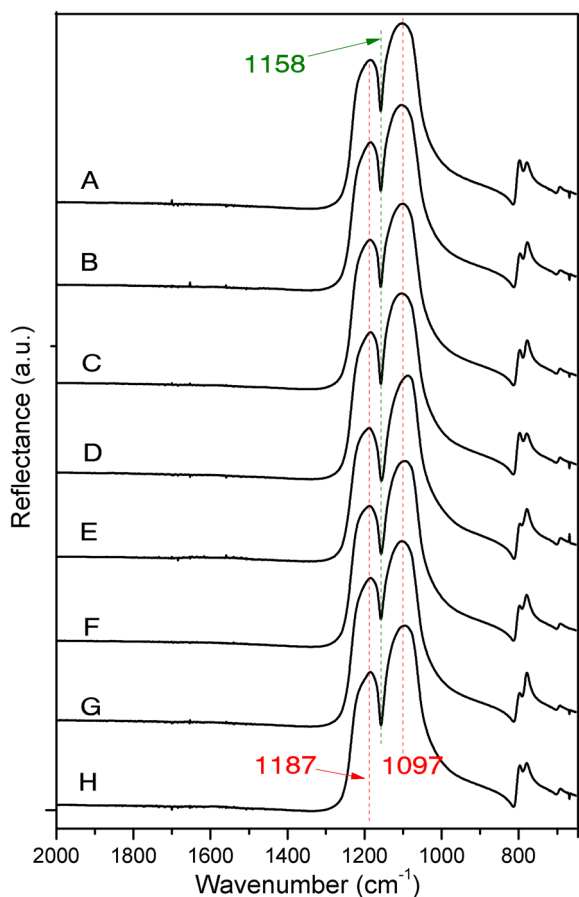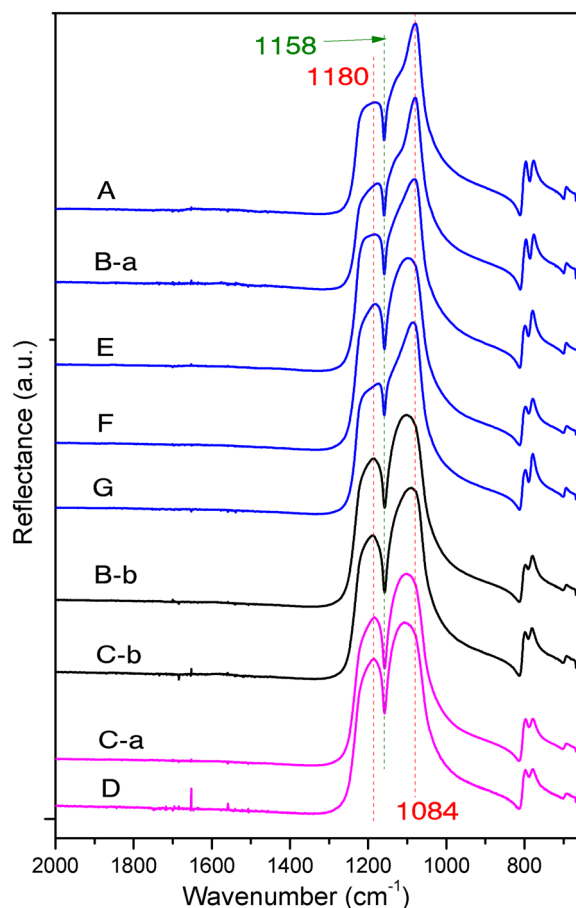
Fig. 7 FTIR spectra of A scattered white zone, B-a scattered white zone, E scattered white zone, F scattered white zone, G scattered white zone, C-a idiochromatic white zone, B-b part translucent zone, C-b part translucent zone, and D idiochromatic white zone

Fig. 6 FTIR spectra of A dark red zone, B black zone, C dark red zone, D black zone, E red zone, F red zone, G red zone, and H red zone

samples A, B-a, E, and G, the FTIR of the scattered white zone of F, the 1097 cm^{-1} peak remains unchanged while the 1187 cm^{-1} peak redshifts (Fig. 7) to 1180 cm^{-1}. This is proposed to be attributed to the grinding and polishing process after etching. The etched pit on F bead was eliminated by grinding, resulting in a slight redshift.

SEM

The SEM images reveal that most of the observed surfaces are flat, which means the beads had been produced by a grinding and polishing process (Fig. 8) [22, 23]. Figure 8i, j show the interface zone between the scattered white and the dark red zones with different magnifications. The scattered white zones always have coarse corrosion surfaces (Fig. 8f and j) compared with the red, the black, and the idiochromatic white zone. Scattered white zones are often lower in elevation than red zones (Fig. 8 i, j). This indicates that the white color was artificially added after polishing. The etching process weakened the
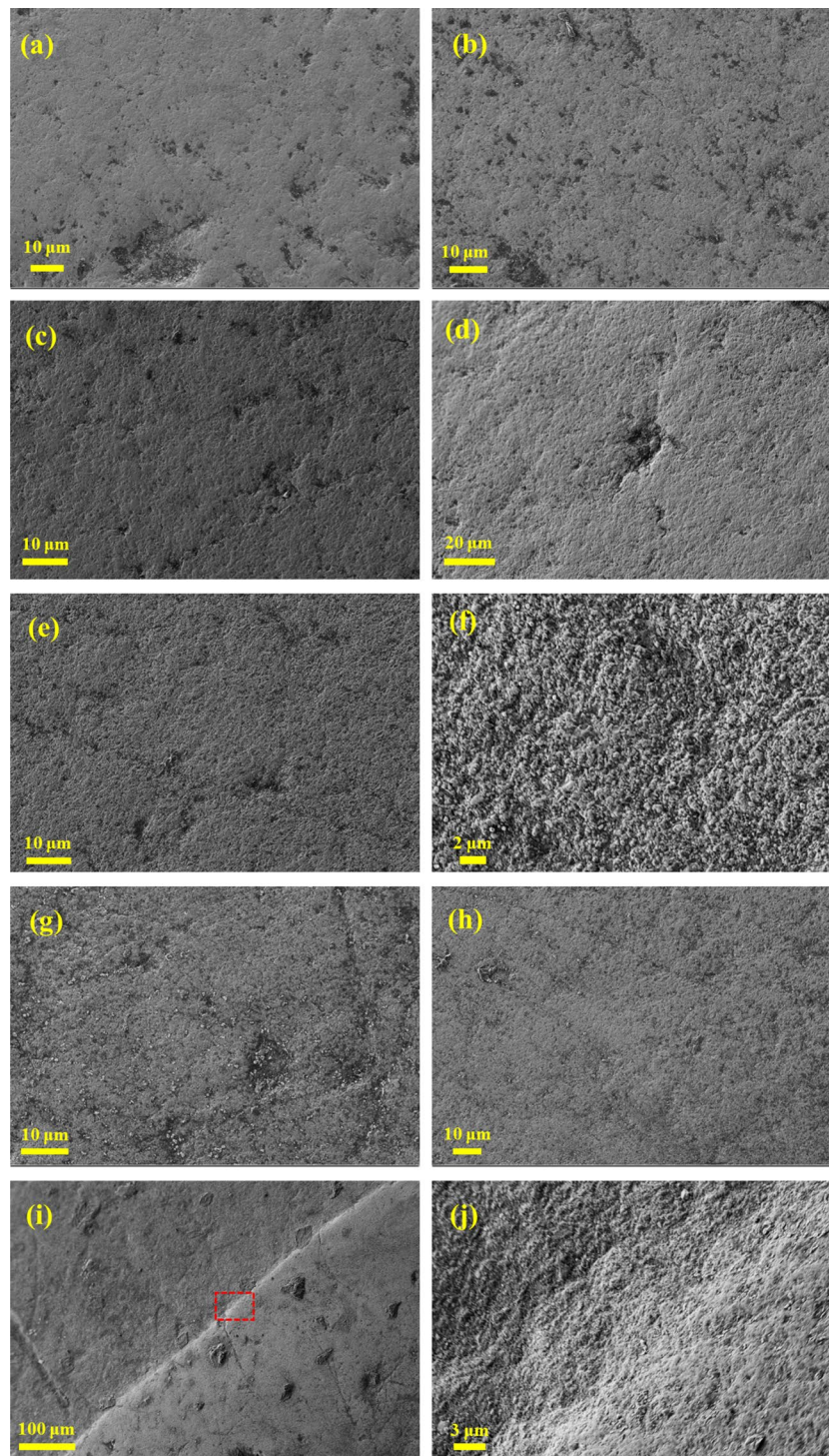
Li *et al. Heritage Science*   (2023) 11:195

Page 7 of 12

Fig. 8 SEM image of (**a**) red black zone of D, (**b**) white zone of D, (**c**) black zone of B, (**d**) translucent zone zone of B, (**e**) white zone of B, (**f**) white zone of B, (**g**) dark red zone of C, (**h**) white zone of C, (**i**) bottom right show the red and left upper zone show the scattered white zone of A, (**j**) the inserted rectangle zone of A in (**i**) with higher magnification

glaze slightly, which may result in a scattered white color. Furthermore, the chemical structure of the agate beads was partially damaged, resulting in a formation of the diffuse reflection surface (Fig. 9).

Discussion

Red and dark red

Beads in this study can be divided into four color categories based on their character and staining mechanism. The first is red, the most common color of the excavated beads.

Natural occurring chalcedonies have different colors and intercrystalline porosities generated by the minor elements and mineral proportions [52, 54]. However, intentional heat treatment of natural agate produces the desired lustre, flaking properties, and the most significant result, red color [22, 33]. Since the structure of natural agate is not compact, the color of agate can be altered by exotic element infiltration into the micropores or subtle channels. Then the iron element in the pores is oxidized to ferric iron to form hematite after heat treatment, supporting the Raman data in this study together with previous literature [68, 69]. Hence, ferric iron is often uniformly present throughout the mineral pores and channels, causing the red color known as carnelian red. In some places with high concentrations, red dots found on the surface of the carnelian indicate the presence of hematite (Fig. 5). The irregular distribution of Fe on the surface of carnelian is caused by the oxidation of the Fe nuclei during the heating process in the bead manufacture or exogenous pollution during burial [6, 60]. Generally, this results in a color change throughout the particle. Therefore, carnelian is the most common material for bead making and is made into various shapes.

The evenly distributed Fe in A may be the source of its dark red color, indicating that these beads may not have undergone a heating process in the air, but are original Fe

Fig. 9 Schematic drawing of etching process observed in side view of the agate surface

cations come from the infiltration of a specific iron-containing liquid. Fe and Mn cations are usually the color-forming elements of natural agate [69–72]. The Fe cations penetrated the surface and spread out across the entire beads.

Although quartz has better crystallinity, it is unsuitable for staining due to its lack of channels. For zone with high crystallinity, the degree of staining will be significantly lower due to the compact crystal structure and smaller pores. This is the formation characteristics of the infiltration-induced red color.

Black

Black-colored agate can form naturally by introducing carbon-bearing material into the porous silica matrix [35]. Continuous black bands can be observed alternating with the white bands, indicating that the black bands were formed successively after or before the white band [73]. Similar to the natural black agate, artificial black-colored beads come from disseminated carbonaceous matter [29, 36, 60, 74]. However, black-colored beads usually appear in a regularly distributed black banded or overall black color type rather than alternating bands, regardless of their natural color bands. The transition boundary between the studied beads' black and white sections clearly cut the agate's concentric zoning bands.

The lack of a line pattern means that the methodology of making the black beads differs from the scattered white beads. This process may be performed by immersing the beads in some kind of liquid. In the iron age, diverse kinds of food, such as honey or sugar, could serve as the carbon source [31]. The black staining process was most probably realized by the organic carbon penetration through the subtle channels in the agate [31, 36]. Because of the principle of penetration, the translucent part of the beads has a slightly different consistency and porosity.

Idiochromatic white and scattered white

Both idiochromatic and scattered white colors appear as common color types of the excavated beads. However, the bead craftsman did not use the same strategies to make idiochromatic white and scattered white beads. The idiochromatic white color comes from the mineral composition that was originally possessed after the quartz formation (Fig. 1, samples C and D). Researchers have found that carnelian beads with a scattered white pattern are clearly due to artificial processing technology rather than an idiochromatic white [1–3, 16, 21, 75]. Some studies have proposed that the scattered white color was generated by the 'micro fractures' of the carnelian surface [8, 31]. Potash and washing soda were believed as an adhesive material for the white carnelian [4, 16, 75]. Some scholars advocate using 'bleaching' since they proposed that the beads are not
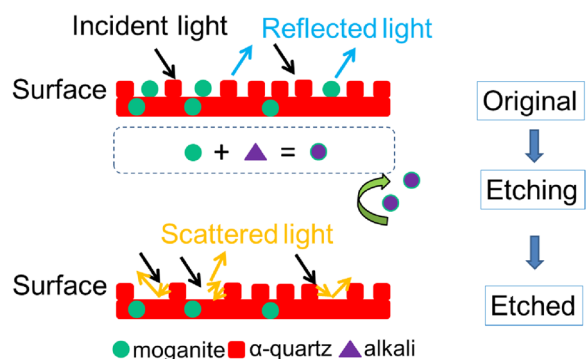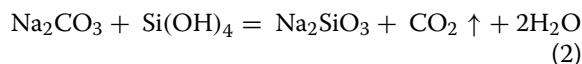
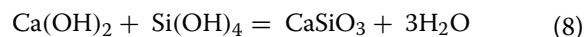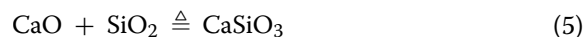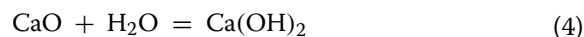Li *et al. Heritage Science*   (2023) 11:195

Page 9 of 12

actually etched but only in a way of white color painting on the red carnelians [1, 38]. According to the μXRF (Table. 2), Raman (Figs. 3, 4), FTIR (Figs. 6, 7), and SEM (Fig. 8) data, we conclude that it is etched into red rather than painted with paint [38, 68]. The pores on the surface of the white zone of agate are irregularly distributed, indicating a corrosion surface. The incident light was scattered by the etched coarse surface of the carnelian, resulting in a white-looking and opaque color.

Generally speaking, the main components of the unearthed beads are α-quartz and moganite. However, the Raman spectrum shows no evidence of moganite peaks in the white zones (Fig. 4). This suggests that the formation of the white color is related to the reaction of moganite. Moganite belongs to the monoclinic crystal system and is generally considered to be an intermediate phase in the transformation of amorphous SiO_2 to crystalline α-quartz [54, 65, 66, 76]. It contains a large number of structural defects in the form of Si-OH, which has greater reactivity than the Si-O bond in α-quartz [77, 78]. Therefore, the chemical reaction should occur first in Si-OH rather than Si-O, although we cannot rule out the reaction of the Si-O bond. Alkali-silica reaction reactions can occur in quartz-bearing rocks [79]. Kirar plant juice was used when producing etched beads without water [4]. However, the washing-soda was proposed to be the active ingredient of the etching liquid rather than the kirar plant juice based on the results of this study [68]. Therefore, moganite is likely to be etched by the following reaction equation (Fig. 9):

$$Na_2CO_3 + SiO_2 \triangleq Na_2SiO_3 + CO_2 \uparrow \qquad (1)$$

$$Na_2CO_3 + Si(OH)_4 = Na_2SiO_3 + CO_2 \uparrow + 2H_2O \qquad (2)$$
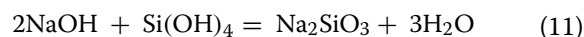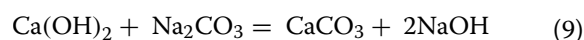
Therefore, our analysis considers that etching is more suitable and accurate for this kind of bead because the moganite was removed by chemical reactivity. Etching rather than bleaching was proposed to be used to accurately describe the carnelian beads because the moganite was removed by chemical reactivity.

In addition to Na, small amounts of K have been detected in μXRF, Na and K can come from etching liquid, and K may also come from plant ash which was made by burning the Amaranth species plant [31] or *kirar* tree [80]. For the prehistoric period, carbonate stone could serve as a Ca source by heating (Eq. 3). Therefore, relatively high levels of the element Ca are likely derived from the $CaCO_3$ in the etching liquid. It may have undergone the following reaction process (Fig. 9):

$$CaCO_3 \triangleq CaO + CO_2 \uparrow \qquad (3)$$

$$CaO + H_2O = Ca(OH)_2 \qquad (4)$$

$$CaO + SiO_2 \triangleq CaSiO_3 \qquad (5)$$

$$CaO + Si(OH)_4 = CaSiO_3 + 2H_2O \qquad (6)$$

$$Ca(OH)_2 + SiO_2 = CaSiO_3 + H_2O \qquad (7)$$

$$Ca(OH)_2 + Si(OH)_4 = CaSiO_3 + 3H_2O \qquad (8)$$

In the presence of calcium hydroxide and sodium carbonate, the following reactions may also produce sodium hydroxide (Fig. 9):

$$Ca(OH)_2 + Na_2CO_3 = CaCO_3 + 2NaOH \qquad (9)$$

$$2NaOH + SiO_2 = Na_2SiO_3 + H_2O \qquad (10)$$

$$2NaOH + Si(OH)_4 = Na_2SiO_3 + 3H_2O \qquad (11)$$

Regardless of the reaction pathway, the etching process is accomplished by breaking Si-O-Si or Si-OH of the moganite to form soluble silicate and carbon dioxide (Fig. 9). According to these results, moganite should be more reactive than α-quartz. In this sense, the temperature will affect the etching rate depending on the moganite proportion and different Si-OH content [51, 54, 81, 82]. Forming a corrosion surface with different depths eventually (Fig. 8f, i, j). A white color can be observed since the rough surface scatters incident light of different wavelengths in all directions.

Conclusions

The identification of the artificial staining mechanisms used on ancient agate beads has been investigated using μXRF, Raman, and FTIR techniques. In this study, systematic mineralogical analyses were conducted on carnelian beads from an Iron Age cemetery on the Pamir Plateau and, for the first time, revealed the different coloration mechanisms of red, black, and white.

In unstained beads, Raman spectroscopic studies revealed a characteristic peak at 502 cm^{-1}, confirming the presence of moganite. All ancient beads with varying colors exhibited similar FTIR features, with variations in peak intensity. The position of the of the 1097 and 1187 cm^{-1} doublet shifted to 1084 and 1180 cm^{-1} with decreasing amounts of moganite. The white zones of samples A, B, E, and G were absent of moganite, which was confirmed by the FTIR data as two prominent peaks that shifted to the low-frequency region compared to the red zone. Higher amounts of Ca and Na were detected using μXRF analyses for the scattered white zone

Li *et al. Heritage Science*   (2023) 11:195

Page 10 of 12

compared to other zones, indicating the etching mechanism of the scattered white color.

Through the application of heating, organic matter infiltration, and alkali etching techniques, beads could be regenerated with a novel appearance to cater to the varied preferences of people from different regions. The red color was produced from a heat treatment, while the black color came from carbonaceous matter infiltration. The scattered white appearance was assigned to the rough and irregular coarse mineral surface that reflected light, resulting from the chemical etching process.

In conclusion, samples C and D belonged to the black-on-idiochromatic white type. The black zones of B and D were manufactured through carbon infiltration, while the white-on-red type samples E, F, G, and H had undergone heat treatment that enhanced the red color and drove the etching reactivity.

The mineralogical study presented in this article is significant for analyzing the geographical spread of agate beads and studying ancient handicrafts. The unique mineral composition and excellent craftsmanship of these colorful ancient beads illustrate a developed pre-historic chemical technology. Further studies may be necessary to better understand the innovation and spread of the color styles and how they might have changed over time.

Availability of data and materials
The original data are shown in the tables and the figures and are available upon request from the authors.

Declarations

Competing interests
None.

References
1. Waele AD, Haerinck E. Etched (carnelian) beads from northeast and southeast Arabia. Arab Archaeol Epigr. 2006;17:31–40.
2. Beck HC. Etched carnelian beads. Antiqu J. 1934;13:384–98.
3. Caspers ED. Etched cornelian beads. London: Bulletin of the Institute of Archaeology; 1971.
4. Mackay E. 150 Decorated carnelian beads. Man. 1933;33:143–6.
5. Koleini F, Colomban I, Pikirayi Prinsloo LC. Glass beads, markers of ancient trade in Sub-Saharan Africa: methodology, state of the art and perspectives. Heritage. 2019;2:2343–69.
6. Kenoyer JM, Cameron A, Bukhchuluun D, Amartuvshin C, Byambat-seren B, Honeychurch W, et al. Carnelian beads in Mongolia: new perspectives on technology and trade. Archaeol Anthropol Sci. 2022;14:1–38.
7. Kristály F, Török B. The role of SiO_2 and silica-rich amorphous materials in understanding the origin of uncommon archeological finds. Mater Manuf Proc. 2020;35:1410–9.
8. Glover IC, Bellina B. Alkaline etched beads East of India in the late prehistoric and early historic periods. Bulletin de l'École française d'Extrême-Orient. 2001;88:191–215.
9. Vaidya S, Mohanty R. Antiquity of bead manufacturing at Mahurjhari and its relevance in early iron age megalithic culture of Vidarbha. J Multidiscip Stud Archaeol. 2015;3:400–9.
10. Carter AK, Abraham SA, Kelly GO. Updating Asia's maritime bead trade: an introduction. Archaeol Res Asia. 2016;6:1–3.
11. Eliyahu BA, Albaz S, Shai I, Maeir AM, Greenfield HJ. Faience beads from early bronze age contexts at tell es-Safi/Gath, Israel. J Archaeol Sci Rep. 2016;7:609–13.
12. Kenoyer J M, Frenez D. Carnelian and Agate Beads in the Oman Peninsula during the Third to Second millennia BC. In the shadow of the ancestors: The prehistoric foundations of the early Arabian civilization in Oman, 2018:397–410.
13. Rawson J. In search of ancient red beads and carved jade in modern China. Cahiers d'Extrême-Asie. 2008;17:1–15. https://doi.org/10.3406/asie.2008.1270.
14. Kenoyer JM. Bead technologies at Harappa, 3300–1900 BC: a comparative summary. South Asian Archaeol. 2001;6:157–70.
15. Francis J. Toward a social history of beadmakers. BEADS J Soc Bead Res. 1994;6:61–80.
16. Glover I, Bellina B. Alkaline etched beads in Southeast Asia. Ornaments from the past: bead study after Beck. Bangkok: Bead Study Trust, London: 2003.p. 92–107.
17. Dong J, Han Y, Ye J, Li Q, Liu S, Gu D. In situ identification of gemstone beads excavated from tombs of the Han Dynasties in Hepu county, Guangxi Province, China using a portable Raman spectrometer. J Raman Spectrosc. 2014;45:596–602.
18. Xia N. Ancient Egyptian beads. Berlin: Springer; 2014.
19. Zhao D. Study on the etched carnelian beads unearthed in China. Chin Archaeol. 2014;14:176–81.
20. Zhao MX. The Hepu Han tombs and the maritime silk road of the Han Dynasty. Antiquity. 2015;88:1229–43.
21. Reade J. Early etched beads and the Indus-Mesopotamia trade: British Museum. Asia: Dept. of West Asiatic Antiquities; 1979.
22. Francis P. Beadmaking at Arikamedu and beyond. World Archaeol. 1991;23:28–43.
23. Kenoyer JM, Vidale M, Bhan KK. Contemporary stone beadmaking in Khambhat, India: patterns of craft specialization and organization of production as reflected in the archaeological record. World Archaeol. 1991;23:44–63.
24. Gwinnett AJ, Gorelick L. Beads, scarabs, and amulets: methods of manufacture in Ancient Egypt. J Am Res Center Egypt. 1993;30:125–32.
25. Kenoyer JM. Trade and technology of the Indus valley: new insights from Harappa, Pakistan. World Archaeol. 1997;29:262–80.
26. Kenoyer JM, Vidale M. A new look at stone drills of the Indus valley tradition. MRS Proc. 1992;267:495.
27. Gardner GB. Ancient beads from the Johore river as evidence of an early link by sea between Malaya and the Roman Empire. J R Asiat Soc. 2011;69:467–70.
28. Dussubieux L, Kusimba CM, Gogte V, Kusimba SB, Gratuze B, Oka R. The trading of ancient glass beads: new analytical data from South Asian and East African soda–alumina glass beads. Archaeometry. 2008;50:797–821.
29. Lankton JW, Diamanti J, Kenoyer JM. A bead timeline. Volume I. 2003:1200
30. Ludvik GE, Kenoyer JM, Klonymus HC, Barkay G, Dvira Z. Stone beads from the temple mount, Jerusalem: a relative chronology through

Li *et al. Heritage Science*   (2023) 11:195

Page 11 of 12

high-resolution studies of bead technology. Archaeol Anthropol Sci. 2022;14:115.

31. Kenoyer JM. History of stone beads and drilling: South Asia. Stone beads of South and Southeast Asia: archaeological, ethnographic and global connections, New Delhi: Aryan Books International,2017.p. 127–50.

32. Kenoyer JM. Culture change during the late Harappan period at Harappa: new insights on Vedic Aryan issues. England: Routledge; 2004.

33. Domanski M, Webb J. A review of heat treatment research. Lithic Technol. 2007;32:153–94.

34. Götze J, Möckel R, Pan Y. Mineralogy, geochemistry and genesis of agate—a review. Minerals. 2020;10:1037.

35. Götze J, Nasdala L, Kempe U, Libowitzky E, Rericha A, Vennemann T. The origin of black colouration in onyx agate from Mali. Mineral Mag. 2012;76:115–27.

36. Svetova EN, Chazhengina SY, Stepanova AV, Svetov SA. Black agates from paleoproterozoic pillow lavas (Onega Basin, Karelian Craton, NW Russia): mineralogy and proposed origin. Minerals. 2021;11:918.

37. Beck HC. Etched carnelian beads: a correction. Antiqu J. 1934;14:65–65.

38. Kenoyer JM. Eye beads from the Indus tradition: technology, style and chronology. J Asian Civiliz. 2013;36:1–22.

39. Bersani D, Lottici pp. Raman spectroscopy of minerals and mineral pigments in archaeometry. J Raman Spectrosc. 2016;47:499–530.

40. Welter N, Schüssler U, Kiefer W. Characterisation of inorganic pigments in ancient glass beads by means of Raman microspectroscopy, microprobe analysis and X-ray diffractometry. J Raman Spectrosc. 2007;38:113–21.

41. Kadlečíková M, Breza J, Gregor M, Bazovský I. Raman spectroscopy of Ancient beads from Devín castle near Bratislava and of four intaglios from other archaeological finds in Slovakia. J Gemmol. 2015:34：510–8. https://doi.org/10.1550/JoG.2015.34.6.510.

42. Akyuz S, Akyuz T, Basaran S, Bolcal C, Gulec A. Analysis of ancient potteries using FT-IR, micro-Raman and EDXRF spectrometry. Vib Spectrosc. 2008;48:276–80.

43. Capel Ferrón C, León-Reina L, Jorge-Villar S, Compaña JM, Aranda MAG, López Navarrete JT, et al. Combined Raman spectroscopic and rietveld analyses as a useful and nondestructive approach to studying flint raw materials at prehistoric archaeological sites. Archaeol Anthropol Sci. 2015;7:235–43.

44. Zhang M, Moxon T. Infrared absorption spectroscopy of SiO_2-moganite. Am Miner. 2014;99:671–80.

45. Wu X, Tang Z. Jirzankal cemetery covered with rows of black-and-white stones: key excavations and primary research. Chin Archaeol. 2016;4:5–82.

46. Li JH, Li QL, Zhao L, Zhang JH, Tang X, Gu LX, et al. Rapid screening of Zr-containing particles from Chang'e-5 lunar soil samples for isotope geochronology: technical roadmap for future study. Geosci Front. 2022;13:101367.

47. Wang X, Tang Z, Wu J, Wu X, Wu Y, Zhou X. Strontium isotope evidence for a highly mobile population on the Pamir Plateau 2500 years ago. Sci Rep. 2016;6:35162.

48. Kenoyer JM. Stone beads in Ancient South Asia-7000–600 BC: A comparative approach to technology, style, and ideology. The Global Perspective of Beads and Beadwork: History, Manufacture, Trade, and Adornment, 2007:1–12.

49. Dalby KN, King L. A new approach to determine and quantify structural units in silicate glasses using micro-reflectance Fourier-Transform infrared spectroscopy. Am Miner. 2006;91:1783–93.

50. Walger E, Mattheß G, Seckendorff V, Liebau F. The formation of agate structures: models for silica transport, agate layer accretion, and for flow patterns and flow regimes in infiltration channels. Neues Jahrbuch für Mineralogie-Abhandlungen. 2009;186/2:113-52. https://doi.org/10.1127/0077-7757/2009/0141.

51. Murashov VV, Svishchev IM. Quartz family of silica polymorphs: comparative simulation study of quartz, moganite, and orthorhombic silica, and their phase transformations. Phys Rev B. 1998;57:5639–46.

52. Schmidt P, Bellot-Gurlet L, Léa V, Sciau P. Moganite detection in silica rocks using raman and infrared spectroscopy. Eur J Mineral. 2013;25:797–805.

53. Rodgers KA, Hampton WA. Laser raman identification of silica phases comprising microtextural components of sinters. Mineral Mag. 2018;67:1–13.

54. Bustillo MÁ, Pérez-Jiménez JL, Alonso-Zarza AM, Furio M. Moganite in the chalcedony varieties of continental cherts (Miocene, Madrid Basin, Spain). Spectrosc Lett. 2012;45:109–13.

55. Caux S, Galland A, Queffelec A, Bordes JG. Aspects and characterization of chert alteration in an archaeological context: a qualitative to quantitative pilot study. J Archaeol Sci Rep. 2018;20:210–9.

56. Hardgrove C, Rogers AD. Thermal infrared and raman microspectroscopy of moganite-bearing rocks. Am Miner. 2013;98:78–84.

57. Briggs RJ, Ramdas AK. Piezospectroscopy of the raman spectrum of quartz. Phys Rev B. 1977;16:3815–26.

58. Ferrari AC, Robertson J, Ferrari AC, Robertson J. Raman spectroscopy of amorphous, nanostructured, diamond–like carbon, and nanodiamond. philosophical transactions of the royal society of London. Ser A Mathem Phys Eng Sci. 2004;362:2477–512.

59. Marshall C, Marshall AO. Hematite and carbonaceous materials in geological samples: a cautionary tale. Spectrochim Acta Part A Mol Biomol Spectrosc. 2011;80:133–7.

60. Dumańska-Słowik M, Powolny T, Sikorska-Jaworowska M, Gaweł A, Kogut L, Poloński K. Characteristics and origin of agates from Płóczki Górne (Lower Silesia, Poland): a combined microscopic, micro-raman, and cathodoluminescence study. Spectrochim Acta Part A Mol Biomol Spectrosc. 2018;192:6–15.

61. Saikia BJ, Parthasarathy G, Sarmah NC. Fourier transform infrared spectroscopic estimation of crystallinity in SiO_2 based rocks. Bull Mater Sci. 2008;31:775–9.

62. Izzo F, Germinario C, Grifa C, Langella A, Mercurio M. External reflectance FTIR dataset (4000–400 cm^{-1}) for the identification of relevant mineralogical phases forming cultural heritage materials. Infrared Phys Technol. 2020;106:103266.

63. Dračínský M, Benda L, Bouř P. Ab initio modeling of fused silica, crystal quartz, and water raman spectra. Chem Phys Lett. 2011;512:54–9.

64. Parthasarathy G, Kunwar AC, Srinivasan R. Occurrence of moganite-rich chalcedony in Deccan flood basalts, Killari, Maharashtra, India. Eur J Mineral. 2001;13:127–34.

65. Perry R, Kolb V, Lynne B, Sephton M, Mcloughlin N, Engel M, et al. How desert varnish forms? Bellingham: SPIE; 2005.

66. Heaney J, McKeown DA, Post JE. Anomalous behavior at the I2/a to Imab phase transition in SiO_2-moganite: an analysis using hard-mode raman spectroscopy. Am Miner. 2007;92:631–9.

67. Schmidt P, Bellot-Gurlet L, Slodczyk A, Fröhlich F. A hitherto unrecognised band in the raman spectra of silica rocks: influence of hydroxylated Si–O bonds (silanole) on the raman moganite band in chalcedony and flint (SiO_2). Phys Chem Miner. 2012;39:455–64.

68. Then-Obłuska J. A few millimeters via thousands of kilometers: an Asian 'etched'carnelian bead in early Makurian Nubia, Sudan. Der Antike Sudan. Mitteilungen der Sudanarchäologischen Gesellschaft zu Berlin e. 2013;24:117–23.

69. Zöldföldi J. Gemstones at Qaṭna royal tomb: preliminary report. Interdisziplinäre Studien zur Königsgruft in Qatna, Edition. 2011;1:234–48.

70. Kickmaier W, Peters T. Manganese occurrences in the Al Hammah Range-Wahrah formation, Oman Mountains. Special Publ. 1990;49:239–49.

71. Cackler R, Glascock MD, Neff H, Iceland H, Pyburn KA, Hudler D, et al. Chipped stone artefacts, source areas, and provenance studies of the Northern Belize Chert-bearing zone. J Archaeol Sci. 1999;26:389–97.

72. Pretola J. A feasibility study using silica polymorph ratios for sourcing chert and chalcedony lithic materials. J Archaeol Sci. 2001;28:721–39.

73. Gliozzo E, Cairncross B, Vennemann T. A geochemical and micro-textural comparison of basalt-hosted chalcedony from the Jurassic Drakensberg and Neoarchean Ventersdorp Supergroup (Vaal River alluvial gravels), South Africa. Int J Earth Sci. 2019;108:1857–77.

74. Allen J. Tibetan dzi beads. Ornament. 1982;6:57.

75. Ebbinghouse D, Winsten M. Tibetan dZi (gZi) Beads. Tibet J. 1988;13:38–56.

76. Moxon T, Rios S. Moganite and water content as a function of age in agate: an XRD and thermogravimetric study. Eur J Mineral. 2004;16:269–78.

77. Schmidt P, Slodczyk A, Léa V, Davidson A, Puaud S, Sciau P. A comparative study of the thermal behaviour of length-fast chalcedony, length-slow chalcedony (quartzine) and moganite. Phys Chem Miner. 2013;40:331–40.

78. Zhang M, Moxon T. In situ infrared spectroscopic studies of OH, H_2O and CO_2 in moganite at high temperatures. Eur J Mineral. 2012;24:123–31.

Li *et al. Heritage Science*   (2023) 11:195

Page 12 of 12

79. Fernandes I, Ramos V, Noronha F, Silva AS, Nunes JC, Medeiros S. Identification of alkali-reactive aggregates: some examples. Proc Inst Civil Eng Const Mater. 2014;167:302–11.

80. Mackay E. Bead making in ancient Sind. J Am Orient Soc. 1937;57:1–15.

81. Götze J, Nasdala L, Kleeberg R, Wenzel M. Occurrence and distribution of moganite" in agate/chalcedony: a combined micro-raman, rietveld, and cathodoluminescence study. Contrib Miner Petrol. 1998;133:96–105.

82. Graetsch H, Flörke OW, Miehe G. Structural defects in microcrystalline silica. Phys Chem Miner. 1987;14:249–57.

Publisher's Note